Supporting Information

Dual-Temperature Photothermal Tandem Catalysis for CO_2 Conversion to Olefins

Ziyang Li[a], Yuhang Qi[a]*, Lipu Han[a], Chu Zhang[a], Zhenwen Yang[a], Zhike Wu[a], Shanshan Xu[b,c]*

[a]School of Electronics and Infomation Engineering, Hebei University of Technology, Tianjin 300130, China.

[b]Department of Materials, School of Natural Science, The University of Manchester, Oxford Road, Manchester M13 9PL, UK
[c]University of Manchester at Harwell, Harwell Science and Innovation Campus, Didcot, Oxfordshire OX11 0DE, UK

Experimental section

1. Materials

Potassium nitrate (KCl, 99.9%), iron(III) nitrate nonahydrate ($Fe(NO_3)_3 \cdot 9H_2O$, 98%), indium(III) nitrate hydrate ($In(NO_3)_3 \cdot xH_3O$, 99.9%), and sodium oleate ($C_{17}H_{33}COONa$, 97%) were purchased from Aladdin Biochemical Technology Co., Ltd. Graphene dispersion (2 mg mL^{-1} in deionized water, >95% purity) was obtained from Nanjing Xianfeng Nano Technology Co., Ltd. All reagents were used as received without further purification.

2. Materials synthesis

Synthesis of K-doped iron oxide (K-Fe_2O_3).

An aqueous KCl solution (0.5 mol L^{-1}) was prepared and added dropwise to $Fe(NO_3)_3 \cdot 9H_2O$ under continuous stirring. The impregnated solid was dried at 80 °C for 24 h and thoroughly ground in an agate mortar. The resulting powder was calcined in a muffle furnace at 450 °C for 2 h in static air with a heating rate of 5 °C min^{-1}. After natural cooling to room temperature, the product was labeled as Fe_2O_3 with a K mass fraction of 2.5%, 5%, 7.5%, and 10% respectively.

Synthesis of pure iron oxide (Fe_2O_3).

$Fe(NO_3)_3 \cdot 9H_2O$ powder was directly calcined in a muffle furnace at 450 °C for 2 h in static air with a heating rate of 5 °C min^{-1}. After natural cooling, the product was labeled as Fe_2O_3.

Synthesis of graphene/indium oxide composite (G-In_2O_3).

Graphene dispersion (2 mg mL^{-1}), $In(NO_3)_3 \cdot xH_2O$, and sodium oleate ($C_{17}H_{33}COONa$) were dispersed in deionized water at a predetermined mass ratio. After magnetic stirring for 2 h to obtain a homogeneous suspension, the mixture was transferred to a 100 mL Teflon-lined stainless-steel autoclave, sealed, and heated at 150 °C for 12 h. The solid product was collected by centrifugation, washed alternately with absolute ethanol and deionized water three times, and dried under vacuum at 60 °C for 12 h. The dried powder was then calcined at 450 °C for 2 h under Ar flow (heating rate 5 °C min^{-1}). After natural cooling, the final product was denoted as G-In_2O_3.

Synthesis of pure indium oxide (In_2O_3).

$In(NO_3)_3 \cdot xH_2O$ and sodium oleate were dispersed in deionized water using the same mass ratio as in the G-In_2O_3 synthesis. The mixture was magnetically stirred for 2 h to form a homogeneous suspension, transferred to a 100 mL Teflon-lined autoclave, and heated at 150 °C for 12 h. The resulting solid was collected by centrifugation, washed alternately with ethanol and deionized water three times, and dried under vacuum at 60 °C for 12 h. The dried powder was then calcined at 450 °C for 2 h under Ar (5 °C min^{-1}). After natural cooling, the sample was denoted as In_2O_3.

3. Reaction conditions and activity evaluation

Photothermal CO_2 conversion with H_2 was carried out in a batch reactor with a total volume of 330 mL. After evacuation, a CO_2/H_2 mixture (H_2/CO_2 molar ratio = 4:1) was introduced. The reaction conditions employed are 0.5 atmospheres. A 300 W Xe lamp was used as the light source to drive the photothermal reaction. The catalyst surface temperature was measured with an infrared thermometer using an emissivity coefficient of 0.78. the amount of gas was controlled through a pressure monitor inside the system. The reactor was kept in the dark for a while to ensure an adsorption−desorption equilibrium of the reactant gases over the catalyst surface; then, the Xe lamp was turned on.

For single-bed tests, 0.05 g of catalyst was uniformly spread onto a circular gas-permeable quartz fiber filter (area 7 cm^2). The filter was fixed on a stage inside the reactor, and the thermometer tip was kept in intimate contact with the catalyst layer (powder thickness ~1–2 mm).

For the dual-bed configuration, G-In_2O_3 and K-Fe_2O_3 were packed in separate layers and separated by an inert screen. The total catalyst loading in the dual bed was 100 mg.

The concentrations of CO_2, CO, CH_4, C_2H_4, C_3H_6, C_2H_6, C_3H_8, and C_4 hydrocarbons in the gas phase were analyzed by gas chromatography (GC-2014, Shimadzu) equipped with a methanizer and flame-ionization detector (FID). Quantification was performed using calibration curves obtained from standard gases.

4. Sample characterization

X-ray diffraction (XRD) patterns were recorded on an X'Pert diffractometer equipped with graphite-monochromatized Cu Kα radiation. Morphologies were examined by field-emission scanning electron microscopy (FE-SEM, Hitachi S-4800) and transmission electron microscopy (TEM, JEOL 2100F). Diffuse-reflectance UV–vis–NIR spectra were measured on a Shimadzu UV-3600 spectrophotometer in the range 220–2400 nm. Surface chemical states were analyzed by X-ray photoelectron spectroscopy (XPS, ESCALAB 250Xi, Thermo Scientific). Photoluminescence (PL) spectra were recorded on a Horiba Fluorolog-3 spectrometer with an excitation wavelength of 350 nm. Electron spin resonance (EPR) spectra were obtained on a JES-FA200 X-band spectrometer. Catalyst temperatures under illumination were monitored using a digital thermometer (Custom CT-1200D). Raman spectra were collected on a Horiba Xplora Plus system. N_2 adsorption–desorption isotherms and pore-size distributions were measured with a BEL Sorp-II mini surface-area analyzer (BET method). FTIR spectra, including in situ measurements, were recorded on a Nicolet 6700 Fourier-transform infrared spectrometer using a conventional IR cell connected to a gas-handling manifold.

Figure section

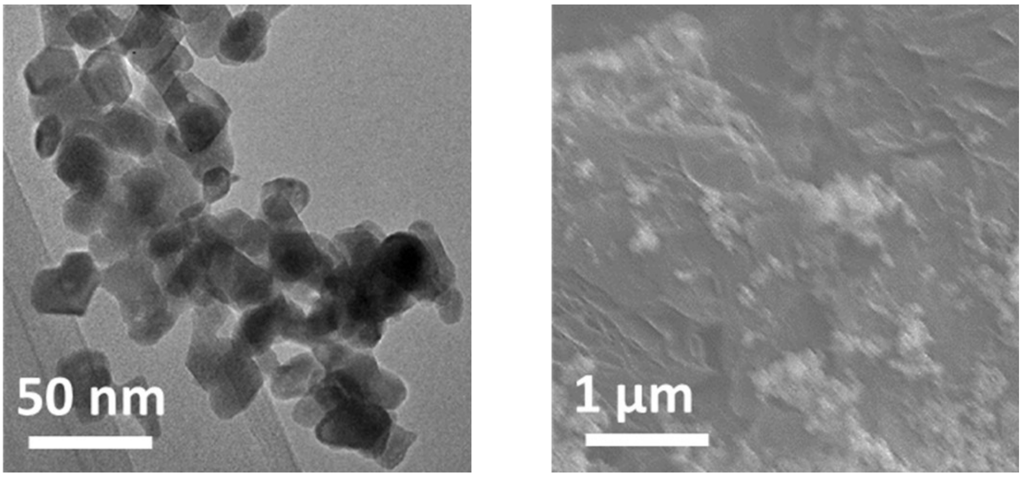

Figure S1. The TEM of In_2O_3, and SEM of G-In_2O_3-10%.

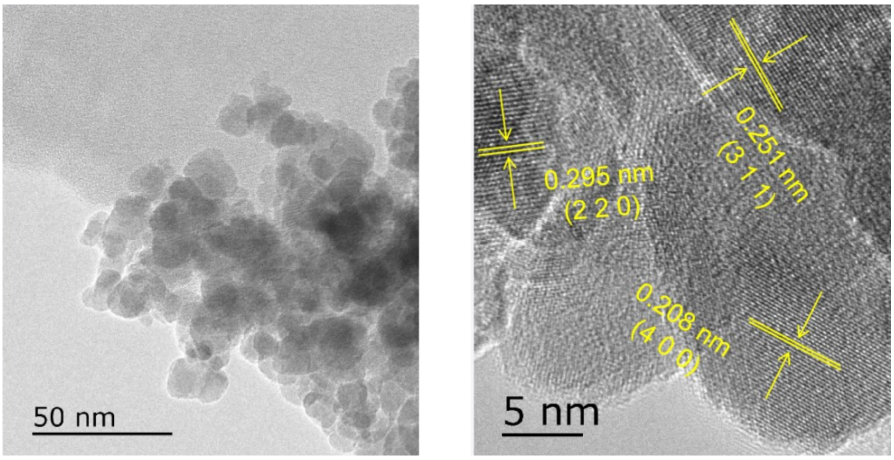

Figure S2. The TEM and HRTEM of Fe_2O_3.

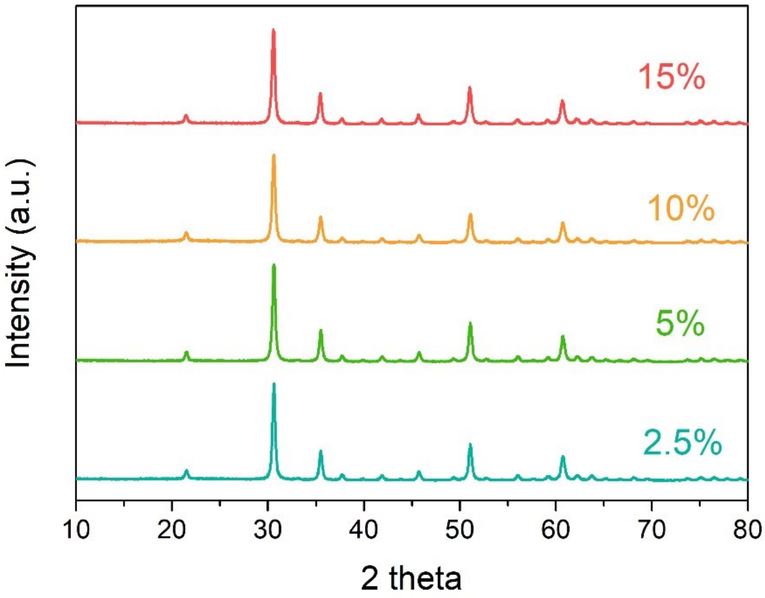

Figure S3. The XRD pattern of In_2O_3 and In_2O_3 with different mass fractions of graphene.

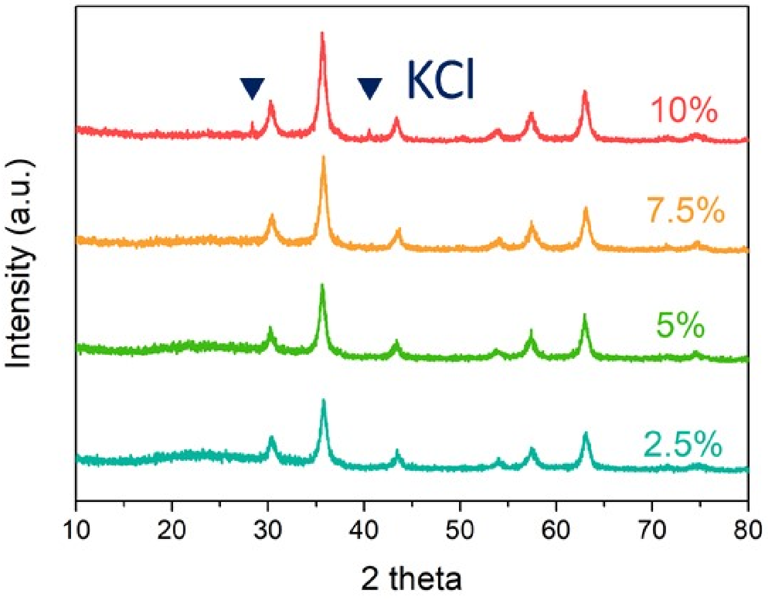

Figure S4. The XRD pattern of Fe_2O_3 and Fe_2O_3 with 2.5%, 5%, 7.5%, 10% mass fractions of K.

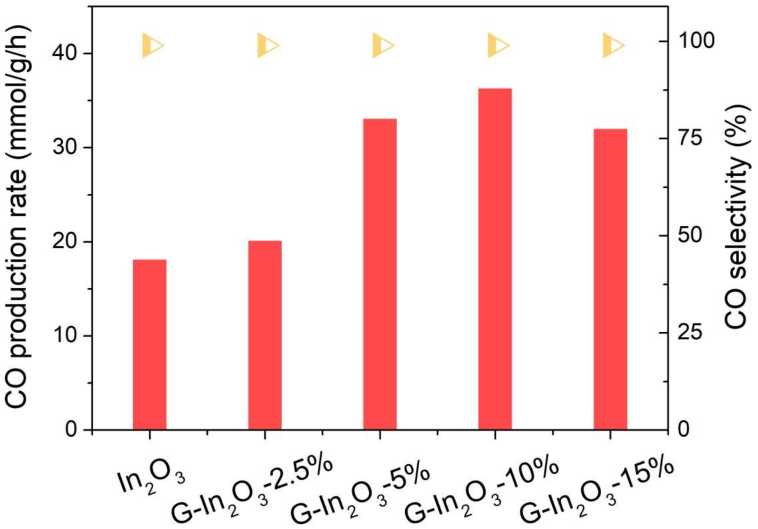

Figure S5. The activity and selectivity of the RWGS reaction of In_2O_3 and In_2O_3 with different mass fractions of graphene.

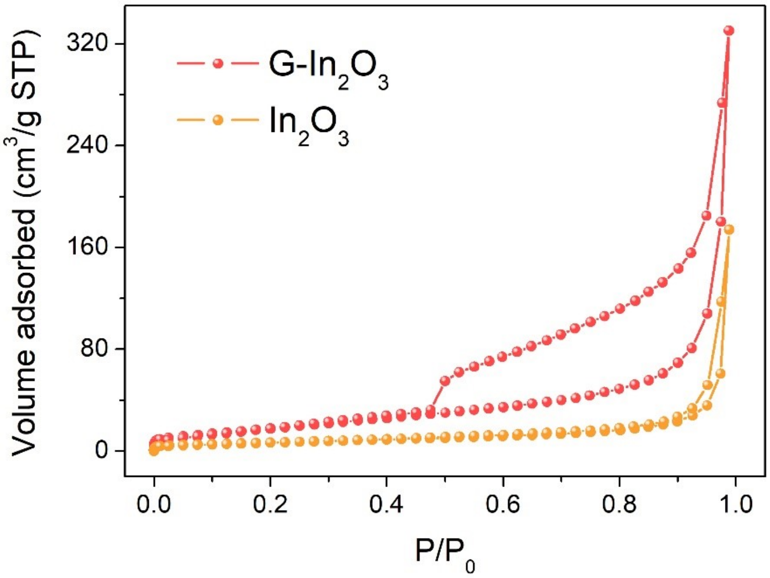

Figure S6. The N_2 adsorption–desorption isotherms of In_2O_3 and G-In_2O_3.

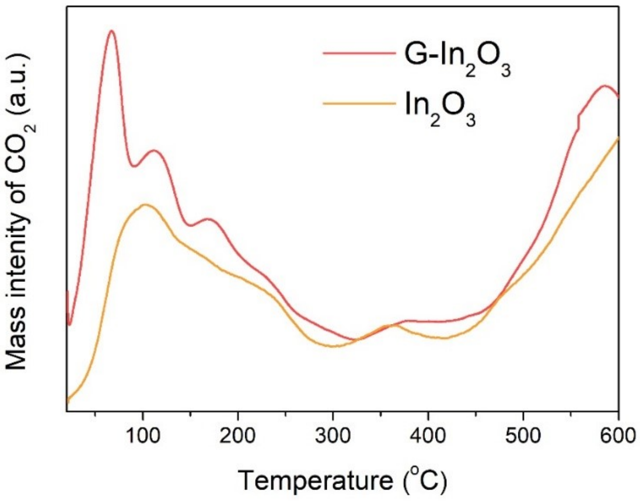

Figure S7. The temperature-programmed desorption of CO_2 from In_2O_3 and G-In_2O_3-10%.

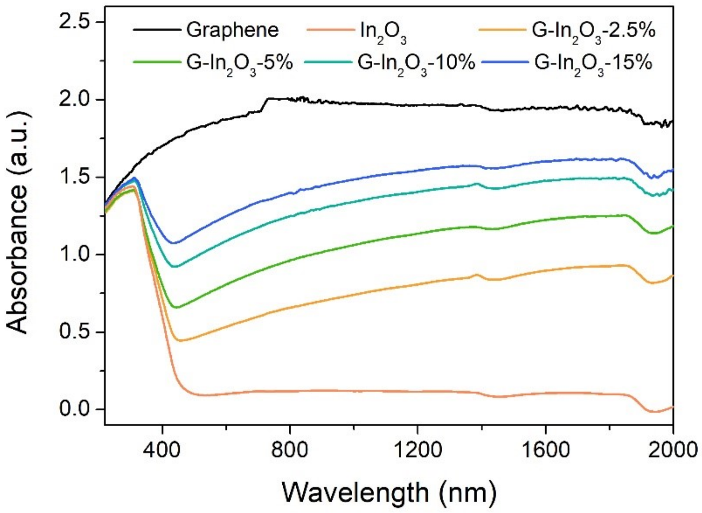

Figure S8. The UV-Vis-NIR spectrum of In_2O_3 and In_2O_3 with different mass fraction graphene.

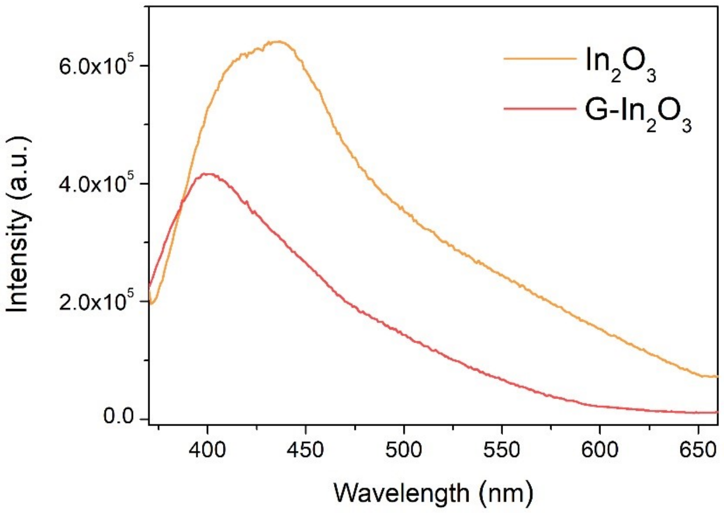

Figure S9. The PL spectrum of In_2O_3 and G-In_2O_3-10%.

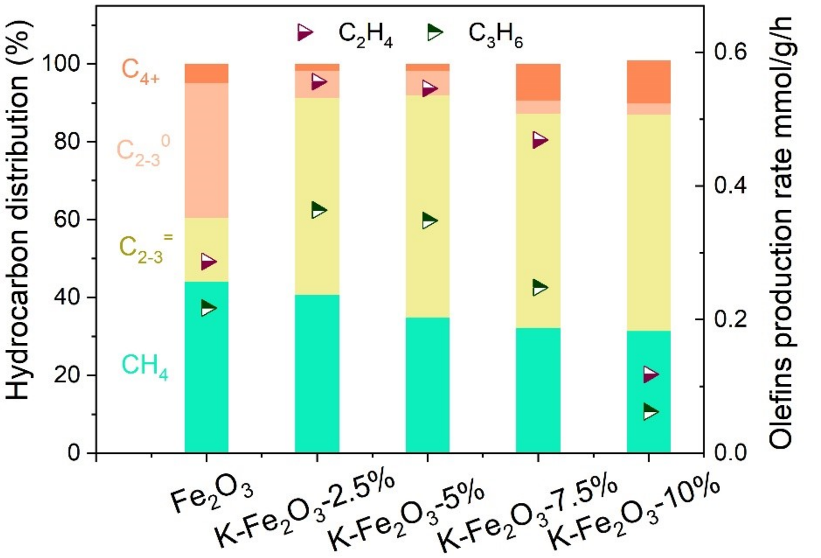

Figure S10. The activity and selectivity of the F-T synthesis of Fe_2O_3 and Fe_2O_3 with different mass fractions of potassium.

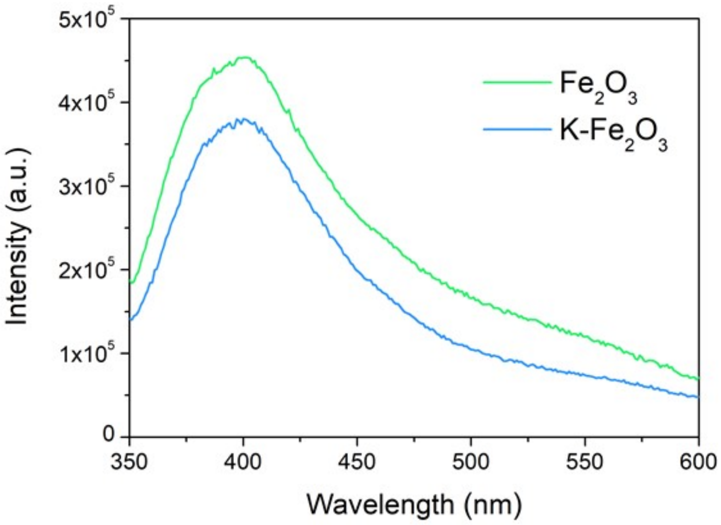

Figure S11. The PL spectrum of Fe_2O_3 and K-Fe_2O_3-5%.

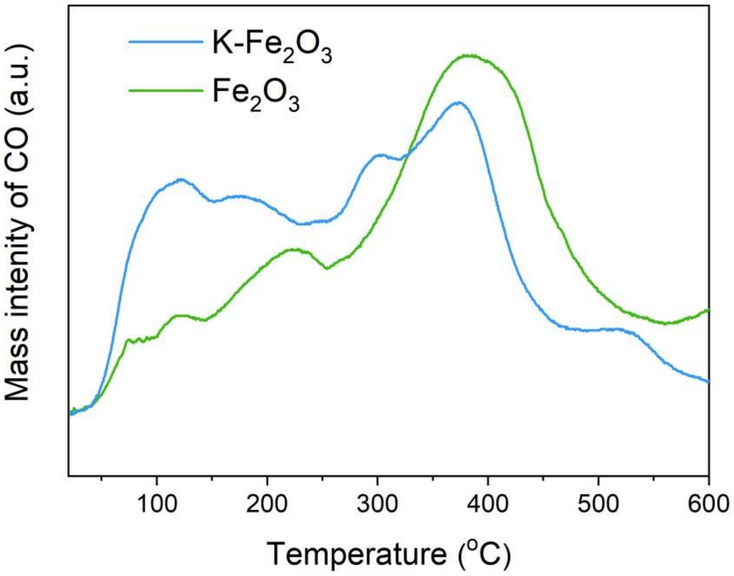

Figure S12. The CO-TPD of Fe_2O_3 and K-Fe_2O_3-5%.

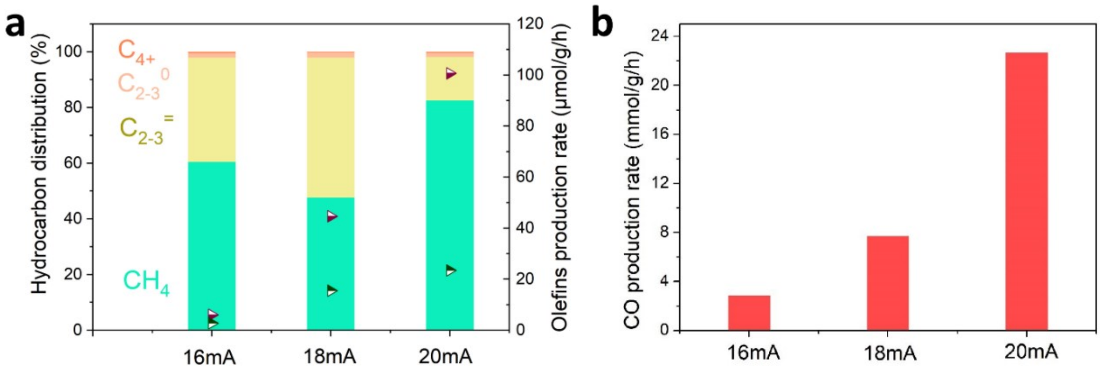

Figure S13. (a)The activity and selectivity of the F-T synthesis of K-Fe_2O_3-5% with different light current, (b) The CO production rate of K-Fe_2O_3-5%with different light current.

As shown in Figure S13a, increasing the photocurrent enhances the light-olefin production rates; however, the olefin selectivity remains essentially unchanged. This behaviour can be attributed to the limited CO concentration generated at low photocurrent (Figure S13b), which restricts its subsequent conversion in the F–T step.

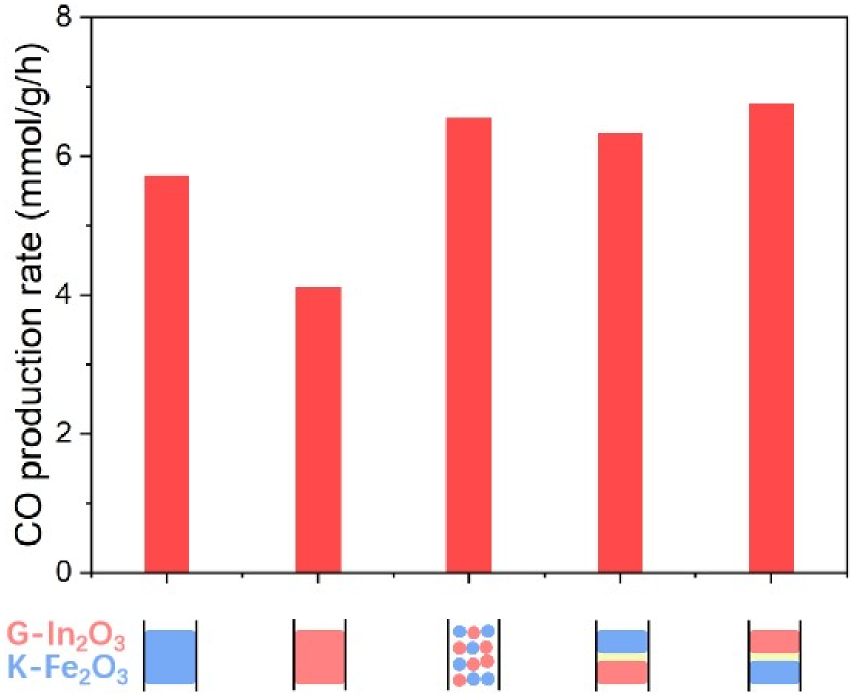

Figure S14. The CO production rate of different integration manners of the active components.

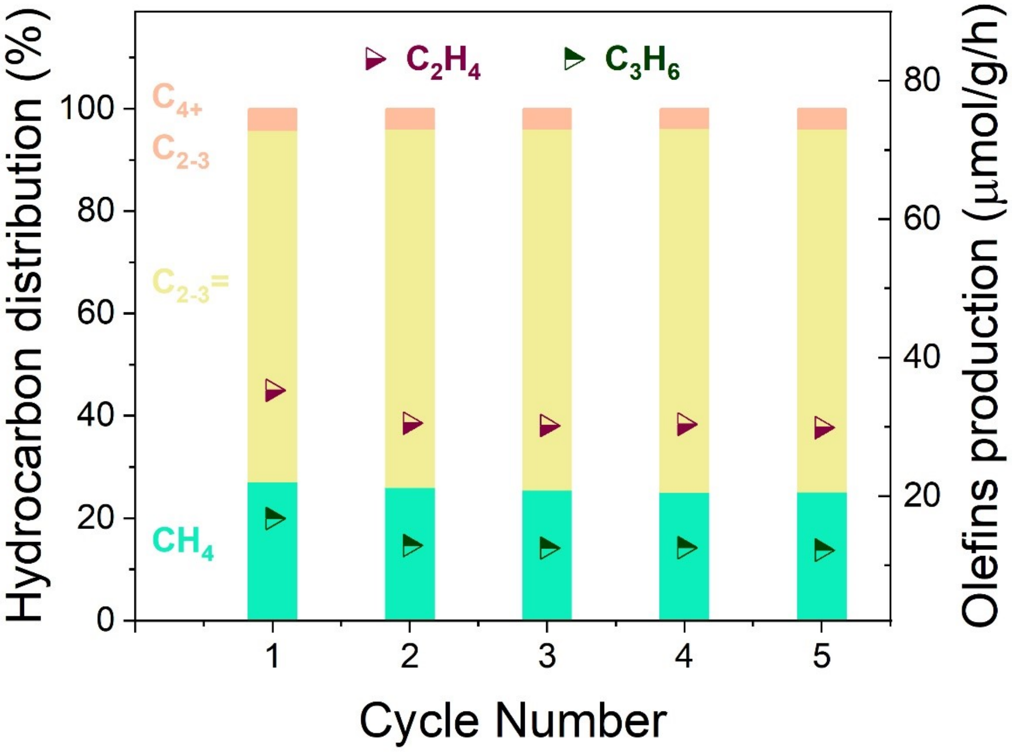

Figure S15. Hydrocarbon distribution and light olefin yield over five consecutive cycles for the tandem catalyst system comprising G-In_2O_3-10% in the upper bed and K-Fe_2O_3-5% in the lower bed (mass ratio = 3:5).

As shown in Fig. S15, the stability of the catalyst system comprising G-In_2O_3-10% in the upper bed and K-Fe_2O_3-5% in the lower bed (mass ratio = 3:5) was evaluated over five consecutive cycles. The hydrocarbon distribution and light olefin yield remained nearly unchanged during the test, indicating good stability of the tandem catalytic system.

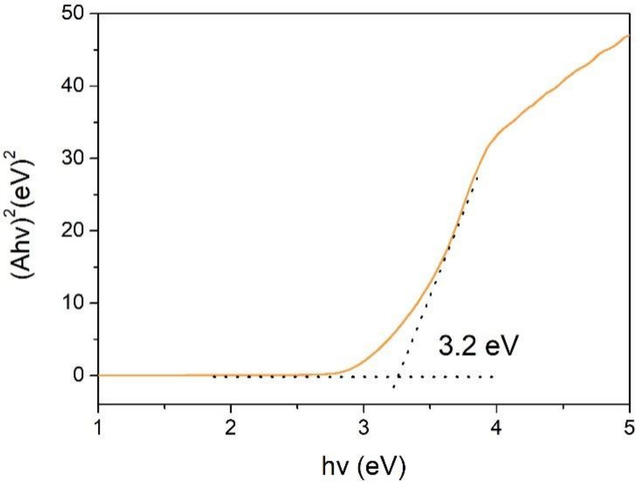

Figure S16. The band gap of In_2O_3.

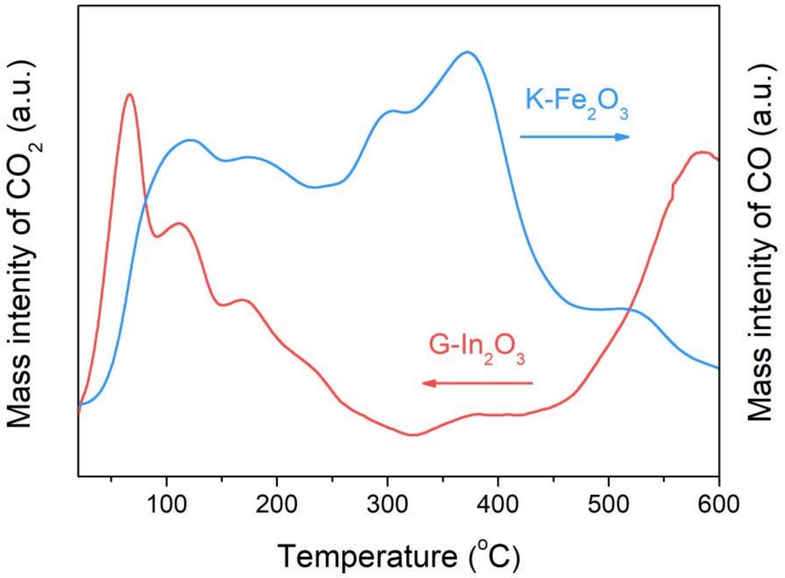

Figure S17. The CO_2-TPD of G-In_2O_3-10% and CO-TPD of K-Fe_2O_3-5%.

This well-defined temperature gradient allows RWGS and FTS to proceed within their respective optimal temperature windows 27, ensuring efficient CO2 adsorption and activation on G-In2O3 and favourable for CO adsorption and chain-growth on K-Fe2O3 (Figure S17).

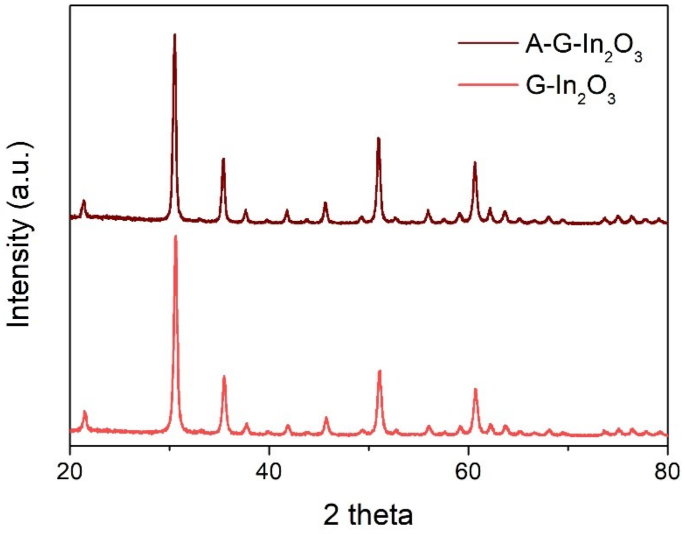

Figure S18. The XRD patterns of G-In_2O_3-10% before and after reaction.

As shown in Figure S18, the XRD patterns remain unchanged, confirming the structural stability.

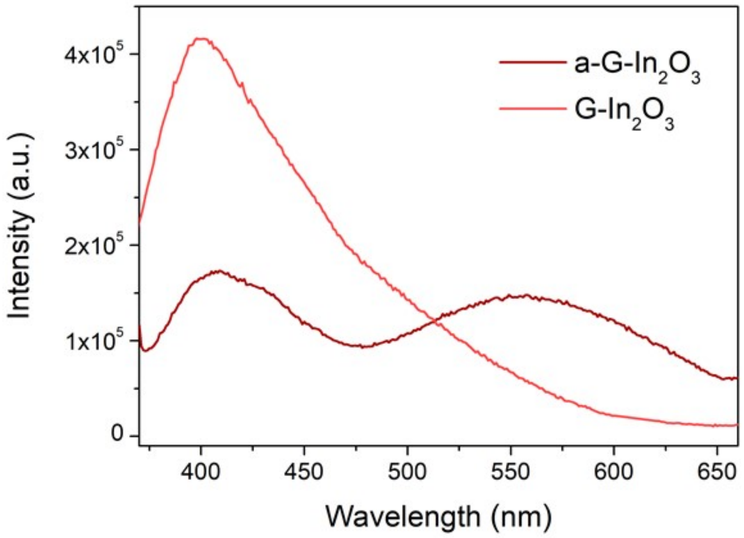

Figure S19. The PL spectrum of G-In_2O_3-10% before and after reaction.

The PL spectrum of fresh G-In_2O_3 exhibits a strong near-band-edge emission at 415 nm and a broad defect-related band centred near 570 nm, characteristic of oxygen-vacancy states (Figure S19).

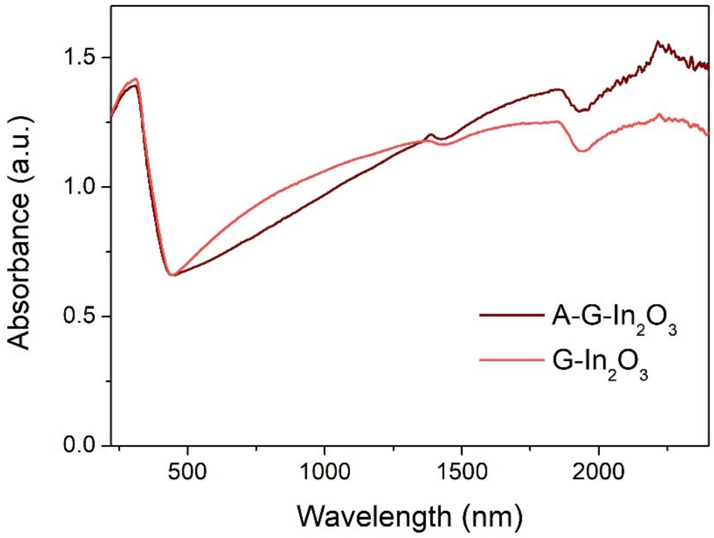

Figure S20. The UV-Vis-NIR spectrum of G-In_2O_3-10% before and after reaction.

After the reaction, the near-band-edge emission is partially quenched, while the defect-related band becomes more intense, suggesting the formation of additional oxygen vacancies and an enhanced interfacial interaction between In_2O_3 and graphene. These vacancies introduce additional energy levels within the band gap, thereby boosting the visible-light absorption of G-In_2O_3, as evidenced by the increased absorbance in the 400–700 nm region of the UV–vis–NIR spectrum (Figure S20).

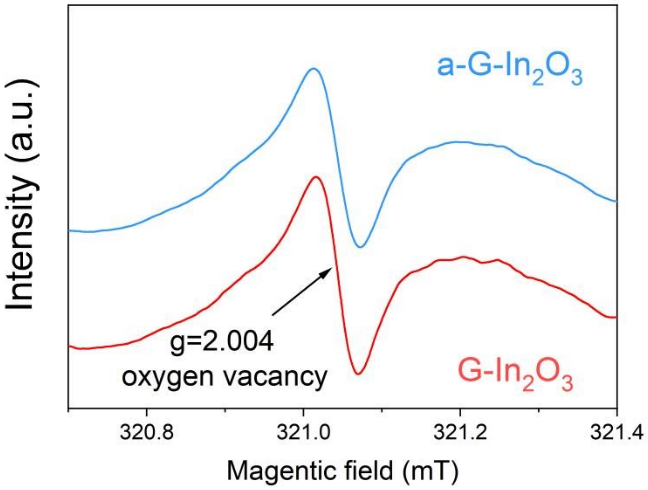

Figure S21. EPR spectra of G- In_2O_3 before and after the reaction.

As shown in Fig. S21, EPR measurements of In_2O_3 before and after reaction confirm the persistence of oxygen vacancies under the reaction conditions. This is likely associated with the H_2-rich and CO-containing atmosphere, which helps maintain the oxygen-deficient state of In_2O_3.

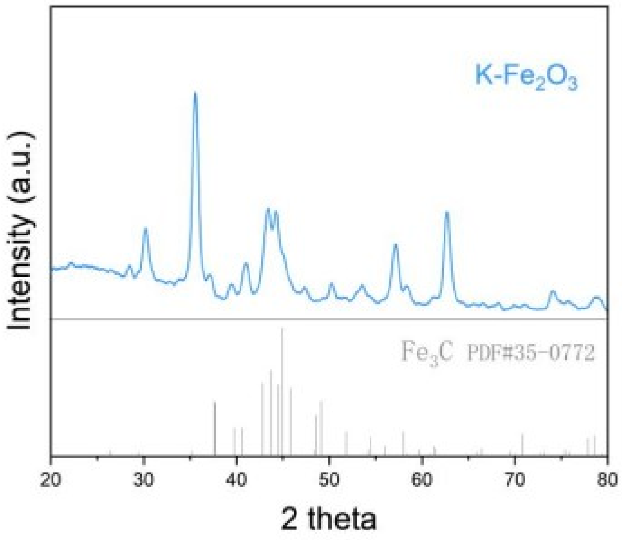

Figure S22. XRD patterns of the after-reaction K-Fe$_2$O$_3$-5% and Fe$_3$C.

Because there is a possibility that Fe$_3$C may form during the activation process leading to the Fe$_5$C$_2$ phase, the post-reaction K-Fe$_2$O$_3$ catalyst was analyzed by XRD and the pattern was compared with the standard PDF card of Fe$_3$C. The results indicate that the active phase does not correspond to Fe$_3$C, thereby excluding the formation of this phase (Figure S22).